Global Stability Analysis for Linear Dynamics

Marek Morzyński, [*]
Bernd R. Noack [†] and Gilead Tadmor [‡]

[*] Institute of Combustion Engines and Transportation Technical University of Poznań, Poznań, Poland
[†] Institut Pprime, CNRS – Université de Poitiers – ENSMA, Département Fluides, Thermique, Combustion, CEAT, Poitiers, France
[‡] Department of Electrical and Computer Engineering, Northeastern University, Boston, MA, USA

Abstract Global stability analysis of fluid flows is presented as a method of extracting physical eigenmodes with associated linear dynamic models. These reduced-order models (ROM) are optimal for the transients near the onset of instability. We describe the computational aspects of the eigenmode extraction in detail. This outline includes (i) the discretization technique of the eigenproblem in the framework of computational fluid dynamics (CFD) and (ii) the solution algorithms for the discretized eigenproblem. As regards physical aspects, the linear ROM are improved by enriching the basis with POD modes and by incorporating weakly nonlinear base flow variations. Results of stability computations are presented for the circular cylinder wake, the flow around a NACA-0012 airfoil and the optimization of passive control. Preliminary 3D eigensolutions show the potential of the global stability method.

1 Introduction

The first pioneering papers on global flow stability (Zebib, 1987; Jackson, 1987) presented a novel method of investigating non-parallel flows. These and other early articles concentrated mainly on critical Reynolds numbers and on the leading eigenvalues comprising growth rates and frequencies. Interest in the corresponding spectrum of physical eigenmodes was small. The opportunities of global stability in designing passive control means was realized from the very beginning but not widely exploited. Active, feedback flow control applications with physical ROM were beyond the scope at that time.

The birth of global stability was possible due to computer power brought by a new generation of vector computers like, for example, the Cray YMP.

Global non-parallel flow stability does not need a frequently employed assumption of a dominating flow direction. It generates a large, fully two- or three-dimensional eigenvalue problem. The new hardware and solution techniques allowed to solve it for the first time for two dimensions. In this way, methods that assume weakly non-parallel flow, being effectively one-dimensional, were enriched by the new approach (Wolter et al., 1989).

The recent period brought a boost of interest in reduced order models (ROM) for various purposes. For example, modern aeroelastics presently uses ROMs of the flow, mode interpolation and many of the techniques described in this chapter. These ROMs serve as cheaper surrogate plants for costly unsteady RANS computations (Lieu et al., 2006; Amsallem and Farhat, 2008). Here, we concentrate on ROM for model based flow control and the role of physical modes in flow modeling.

Flow control is a key technology in improving the performance of transport systems, like cars, trains and airplanes. Actuators may be operate in passive, active open-loop or active closed-loop mode. The latter variant may be considered as the most general type of control. The potential of closed-loop flow control is increasingly realized and exploited (Becker et al., 2002). A systematic control-theoretical treatment of flow control has actively been pursued since one decade. The review article (Theofilis, 2003) serves as a good starting point for a more detailed reading. The use of model-based feed-back control, requires low dimensionality of the model for online capability and robustness (see chapter of R. King in this volume). POD modes, being the result of pure signal processing, were used in early days of flow modeling are now enriched by numerous novel and interesting improvements (Bergmann et al., 2005; Deane et al., 1991; Jørgensen et al., 2003; Khibnik et al., 2000; Ma and Karniadakis, 2002; Siegel et al., 2006). The more successful ROM approaches typically incorporated more physical information about the modeled system. The need for new methods in flow modeling enhanced interest also in global stability method and led to development of new tools (Schmid and Sesterhenn, 2008; Rowley et al., 2009). In (Åkervik et al., 2007; Bagheri et al., 2009), control design employs stability modes.

This chapter is organized as follows. After a description of the global stability problem in § 2, computational aspects are outlined, namely the FEM discretization in § 3 and iterative eigensolvers in § 4. Results for the cylinder wake are presented for the natural wake stability (§ 5) and control design (§ 6). In § 7, we outline the role of nonlinearity for dynamic model development.

2 Global flow stability analysis

We consider the flow stability problem for the incompressible fluid motion in a Cartesian coordinate system (x_1, x_2, x_3). The velocity vector (u_1, u_2, u_3) comprises components in these three coordinate directions. The pressure is denoted by p. We assume that all quantities are non-dimensionalized with scale D, velocity U and density ρ. The flow properties are thus characterized by the Reynolds number $Re = UD/\nu$, ν being the kinematic viscosity of the fluid.

The fluid motion is described by the incompressibility condition

$$u_{i,i} = 0$$

and the unsteady Navier-Stokes equation:

$$\dot{u}_i + u_{i,j}u_j + p_{,i} - \frac{1}{Re}u_{i,jj} = 0. \tag{1}$$

Here and henceforth, we apply the summation convention for double indices. The subscripts $',j$' and $',jj$' denote the first and second derivatives in j-th direction and $\dot{u}_i$ is the time derivative of u_i, respectively.

We decompose the unsteady solution of the Navier-Stokes equation (1) as the sum of its steady solution (indicated by the bar) and the disturbance (indicated by the prime):

$$\begin{aligned} u_i &= \bar{u_i} + \acute{u_i}, \\ p &= \bar{p} + \acute{p}. \end{aligned}$$

This decomposition leads us to the disturbance equation in the form:

$$\dot{\acute{u_i}} + \acute{u}_j\bar{u}_{i,j} + \bar{u}_j\acute{u}_{i,j} + \acute{u}_j\acute{u}_{i,j} + \acute{p}_{,i} - \frac{1}{Re}\acute{u}_{i,jj} = 0 \tag{2}$$

and the continuity equation for the disturbance:

$$\acute{u}_{i,i} = 0. \tag{3}$$

We consider the global non-parallel flow stability, yielding global eigenmodes. None of the spatial direction is distinguished. In particular, we do not assume any *dominating flow direction* or *weakly non-parallel flow*. This is the most general assumption of linear stability theory. Under non-degenerate conditions, the evolution of any infinitesimal disturbance is composed of normal solutions with product ansatz for space and time dependency:

$$\begin{aligned} \acute{u}_i(x, y, z, t) &= \tilde{u}_i(x, y, z)\, e^{\lambda t}, \\ \acute{p}(x, y, z, t) &= \tilde{p}(x, y, z)\, e^{\lambda t}. \end{aligned} \tag{4}$$

A traveling wave may appear as a *solution* of the problem but is form is not pre-assumed.

To formulate a differential eigenvalue problem, we linearize the equation (2), i.e. we ignore the quadratic term $\acute{u}_j \acute{u}_{i,j}$. In this linearized disturbance equation, we separate the time and space dependence according to (4).

Introducing (4) into the linearized form of (2) results in a linear system of partial differential equations:

$$\lambda \tilde{u}_i + \tilde{u}_j \bar{u}_{i,j} + \bar{u}_j \tilde{u}_{i,j} + \tilde{p}_{,i} - \frac{1}{Re} \tilde{u}_{i,jj} = 0,$$
$$\tilde{u}_{i,i} = 0. \tag{5}$$

Equation (5) represents the generalized differential eigenvalue problem.

3 Finite Element Method discretization of the global flow stability problem

We use the Finite Element Method with its penalty formulation for discretization of the Navier-Stokes equation (1) and for the eigenvalue problem (5). Fluid velocity is expressed by sums of the quadratic interpolation functions:

$$u_i = \Phi_k u_{ik}. \tag{6}$$

The index sets for i, k are $i = 1, 2$; $k = 1, \ldots, 6$ for 2D and $i = 1, 2, 3$; $k = 1, \ldots, 10$ for 3D. The interpolation function is defined on a 6-node triangular or 10-node tetrahedral element depicted in Fig. 1.

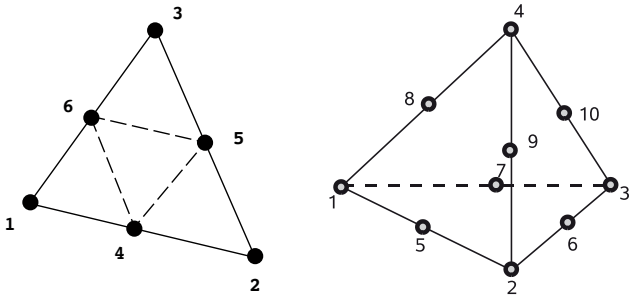

Figure 1. Natural coordinate triangular and tetrahedral element with quadratic interpolation function

The penalty method eliminates the pressure from governing equations via:

$$\frac{1}{\epsilon}p = u_{i,i}. \tag{7}$$

The penalty FEM approach is described in detail in (Baker, 1983; Chung, 2002). The penalty parameter ϵ is usually chosen to be a large number, related to computer word length. Sometimes it is varied within the iteration process to increase the convergence rate. Numerical experiments show that variation of ϵ in the range of 10^3–10^7 has negligible influence on the steady flow solutions. In the calculations presented in the following sections, we assume $\epsilon = 10^5$ and keep it constant in the iteration process. In mixed (velocity-pressure) FEM formulation poor conditioning of the linear equation system can be avoided with an interpolation function for pressure of lower order as compared to the velocity one. In penalty formulation, we apply a similar technique and assume linear interpolation of velocity in the penalty term and a quadratic interpolation in all other terms.

First, we have to find the steady solution for the flow eigenanalysis. We present the FEM procedure in detail, since it is very similar to the eigensolver one. The approximation residual $R_i^{(1)}$ of the steady Navier-Stokes equation with FEM approximation (6) reads:

$$u_{i,j}u_j + p_{,i} - \frac{1}{Re}u_{i,jj} = R_i^{(1)}. \tag{8}$$

We introduce a set of weighting functions w_i and evaluate the standard inner product $(R_i^{(1)}, w_i)$ on each triangular or tetrahedral volume element. With the Galerkin method

$$(R_i^{(1)}, w_i) = 0, \tag{9}$$

we formulate the FEM discretization:

$$\int_\Omega \left(u_{i,j}u_j + p_{,i} - \frac{1}{Re}u_{i,jj} \right) \Phi_m \, d\Omega = 0. \tag{10}$$

We employ the interpolation functions for the velocity field and obtain

$$\int_\Omega \left(\Phi_{k,j}u_{ik}\Phi_o u_{jo} + p_{,i} - \frac{1}{Re}\Phi_{k,jj}u_{ik} \right) \Phi_m \, d\Omega = 0. \tag{11}$$

The equation (11) is used to calculate the element matrices. Further, we exploit the weak formulation of the problem. This allows a lower differentiation order of weighting and interpolation functions and delivers a very

convenient stress–free natural boundary condition. In this formulation, we apply the Gauss-Green theorem to the diffusion term:

$$\int_\Omega u_{ik}\Phi_{k,jj}\Phi_m \, d\Omega = \int_\Gamma \Phi_m u_{i,j} n_j \, d\Gamma - \int_\Omega u_{ik}\Phi_{k,j}\Phi_{m,j} \, d\Omega. \tag{12}$$

The same procedure is applied to the pressure term:

$$\int_\Omega p_{,i}\Phi_m \, d\Omega = \int_\Gamma p\Phi_m \delta_{ij} n_j d\Gamma - \int_\Omega p\Phi_{m,i} \, d\Omega. \tag{13}$$

With the penalty function given by (7), we obtain the final version of the FEM equation:

$$u_{ik}u_{jo}\int_\Omega \Phi_{k,j}\Phi_o\Phi_m \, d\Omega - \epsilon u_{jk}\int_\Omega \Phi_{k,j}\Phi_{m,i} \, d\Omega - \int_\Gamma \Phi_m(-p\delta_{ij} + \frac{1}{Re}u_{i,j})n_j d\Gamma + \frac{1}{Re}u_{ik}\int_\Omega \Phi_{k,j}\Phi_{m,j} \, d\Omega = 0. \tag{14}$$

For triangular and tetrahedral elements it is possible to integrate the FEM matrix exactly with formulas given in FEM textbooks (see, e.g., (Chung, 2002; Baker, 1983)). For this purpose, we use the symbolic manipulation program REDUCE. For example, element $A(1,1)$ for the 3D case is given by:

```
 a(1,1)=(re*vol*(2*ux(10)*b1+4*ux(10)*b3+4*ux(10)*b4+2*ux(9)*b1
. +4*ux(9)*b2+4*ux(9)*b4+8*ux(8)*b1+12*ux(8)*b4+8*ux(7)*b1+12*ux
. (7)*b3+2*ux(6)*b1+4*ux(6)*b2+4*ux(6)*b3+8*ux(5)*b1+12*ux(5)*b2
. -ux(4)*b1-2*ux(4)*b4-ux(3)*b1-2*ux(3)*b3-ux(2)*b1-2*ux(2)*b2+
. 12*ux(1)*b1+2*uy(10)*c1+2*uy(9)*c1+4*uy(8)*c1+4*uy(7)*c1+2*uy(
. 6)*c1+4*uy(5)*c1-uy(4)*c1-uy(3)*c1-uy(2)*c1+6*uy(1)*c1+2*uz(10
. )*d1+2*uz(9)*d1+4*uz(8)*d1+4*uz(7)*d1+2*uz(6)*d1+4*uz(5)*d1-uz
. (4)*d1-uz(3)*d1-uz(2)*d1+6*uz(1)*d1+252*b1**2*eps)+252*vol*(b1
. **2+c1**2+d1**2))/420
```

The equation (14) is nonlinear. We define the residual vector as:

$$R_i(u) := F_{ij}(u)u_j \tag{15}$$

We solve the nonlinear steady-state equation with the Newton–Raphson method for the linearized equation. Introducing the Jacobian $J_{ij}^{(0)}$ and the guess solution $u^{(0)}$:

$$J_{ij}^{(0)} = \frac{\partial R_i(u^{(0)})}{\partial u_j}, \tag{16}$$

we obtai n the expression for the correction of the solution in the subsequent iteration:

$$J_{ij}^{(0)}\Delta u_j = -R_i(u^{(0)}). \tag{17}$$

This linear equation is solved iteratively until the desired accuracy is obtained.

By analogy with the steady flow equation, we can derive the penalty-formulation FEM equation for the eigenvalue problem:

$$\lambda \int_\Omega \Phi_k \tilde{u}_i \, d\Omega + \int_\Omega \Phi_k \left[\tilde{u}_j \bar{u}_{i,j} + \bar{u}_j \tilde{u}_{i,j} + \tilde{p}_{,i} \right] d\Omega - \frac{1}{Re} \int_\Omega \Phi_k \tilde{u}_{i,jj} \, d\Omega = 0.$$

After integration we obtain:

$$\begin{aligned} \lambda \tilde{u}_{im} \int_\Omega \Phi_k \Phi_m \, d\Omega + (\tilde{u}_{ik} \bar{u}_{jo} + \bar{u}_{ik} \tilde{u}_{jo}) \int_\Omega \Phi_{k,j} \Phi_o \Phi_m \, d\Omega \\ - \epsilon \tilde{u}_{jk} \int_\Omega \Phi_{k,j} \Phi_{m,i} \, d\Omega \qquad (18) \\ - \int_\Gamma \Phi_m (-\tilde{p} \delta_{ij} + \frac{1}{Re} \tilde{u}_{i,k}) n_j d\Gamma + \tilde{u}_{ik} \frac{1}{Re} \int_\Omega \Phi_{k,j} \Phi_{m,j} \, d\Omega = 0. \end{aligned}$$

This equation represents the generalized complex, non-Hermitian eigenvalue problem:

$$\mathbf{A}\mathbf{x} - \lambda \mathbf{B}\mathbf{x} = \mathbf{0} \qquad (19)$$

4 Numerical techniques to solution of the eigenvalue problem

Before attempting to solve equation (19), let us consider the possible approaches for the linearized equation (2). We intend to identify the eigenmodes and eigenvalues for this dynamical system. Model (2) is a *white–box* system and we can use a discretized eigenvalue problem (19) to find an eigensolution. The alternative method of system identification is known as the *black–box* method. One can exemplify these approaches considering identification of eigenmodes in aeroelasticity. If the structural model of the airplane is available, we can use the FEM (*white–box* model) to compute the normal modes necessary for aeroelastic analysis. However, an alternative procedure is often used in the ground tests. We have the airplane but the complete technical documentation is unavailable. The modes for aeroelastic analysis are needed to asses the necessary modifications, e.g. change of the stores. Now, in the ground test, we force the (*black–box*) system and record the answers. Postprocessing of these measurements gives the required eigensolutions. The latter method also be used also for the linearized equation (2). We concentrate then on the flow snapshots generated by unsteady integration of this equation and try to identify the empirical

eigenmodes of the system. The results presented in following chapters are based only on solution of the algebraic eigenvalue system. As this black-box method is intensively developed recently (Rowley et al., 2009; Schmid and Sesterhenn, 2008), the time domain system identification is presented briefly in § 4.4.

4.1 Solution of Algebraic Eigenvalue Problem

Equation (19) represents a non-Hermitian, generalized eigenvalue problem. The matrices are unsymmetrical, not positive definite, large and sparse. The solution of large eigenproblems is not trivial, even in case of Hermitian matrices. Here, the solution is even more difficult. The algorithms (e.g. QZ) of library routines (like EISPACK) are not suitable for solution, even in two-dimensional case. We can relay only on iterative solvers. Iterative methods are based on determination of both the eigenvalue and the eigenvector at the same time. The simplest power method for the eigenproblem

$$\mathbf{A}\mathbf{x} = \lambda\mathbf{x} \tag{20}$$

starts the solution from the random vector $\mathbf{x}$. Computation of $\mathbf{A}^2\mathbf{x} = \mathbf{A}(\mathbf{A}\mathbf{x}) \sim \lambda^2\mathbf{x}$ then $\mathbf{A}^3\mathbf{x} = \mathbf{A}(\mathbf{A}^2\mathbf{x}) \sim \lambda^3\mathbf{x}$ and finally, $\mathbf{A}^n\mathbf{x} = \mathbf{A}(\mathbf{A}^{n-1}\mathbf{x}) \sim \lambda^n\mathbf{x}$ enables determination of the largest eigenvalue λ of the matrix $\mathbf{A}$.

If we are interested in several eigenvalues we can reduce the system (19) exactly in the same way as model reduction of large linear dynamic systems is performed. We define a projection of the high dimensional space to a lower dimensional one for which we intend to build a model which preserves principal dynamics properties:

$$\mathbf{\Theta}^T\,\mathbf{B}\,\mathbf{\Theta}\,\dot{\mathbf{x}_r} = \mathbf{\Theta}^T\,\mathbf{A}\,\mathbf{\Theta}\,\mathbf{x}_r \tag{21}$$

where $\mathbf{x} = \mathbf{\Theta}\,\mathbf{x}_r$ and r denotes the reduced system having a dimension m which is much smaller then the original one (19). For the projection, we use the Krylov subspace, spanned by m vectors and defined as:

$$\mathbf{K}_m = [\mathbf{x}, \mathbf{A}\mathbf{x}, \mathbf{A}^2\mathbf{x}, ..\mathbf{A}^{m-1}\mathbf{x}]. \tag{22}$$

To assure that the vectors constituting the Krylov subspace are linearly independent, Gram–Schmidt orthogonalization is usually used. Instead of a single vector in the power method, we compute now several vectors simultaneously. The vectors of Krylov subspace converge now to n dominating eigenvectors of $\mathbf{A}$. The stabilized version of the Krylov subspace algorithm is Arnoldi method, the most often used eigensolver procedure for the global flow stability.

The power method converges to the largest eigenvalue of $\mathbf{A}$ while we are interested in the smallest one, more precisely in the rightmost having the smallest real part of the complex eigenvalue. If we substitute $\mathbf{A}$ with $\mathbf{A}^{-1}$ the power method is now the inverse iteration method and gives us the desired eigensolution. In practice we do not invert matrix $\mathbf{A}$ but use the LU decomposition. For subspace iteration the procedure is similar, but now we compute m eigenvalues and eigenvectors simultaneously.

4.2 Subspace iteration method

Technically, the subspace iteration is a natural extension of the power method to m eigensolutions instead of one. We can iterate in direct or inverse mode finding the largest or the smallest eigenvalues.

Physically, the concept of the method is to reduce the system for which the eigenvalues have to be calculated to another one, with less degrees of freedom, for which eigensolution can be found much easier.

In subspace iteration, the first step is to assign initial values to the elements of m linearly independent vectors. In practice we use the orthogonal vectors obtained by setting unit value to a zero vector. In this way the orthogonality condition is easily fulfilled:

$$\mathbf{R}^{(0)} = \left[\mathbf{R}_1^{(0)}, \mathbf{R}_2^{(0)}, \mathbf{R}_3^{(0)}, ...\mathbf{R}_m^{(0)}\right]. \tag{23}$$

It should be noted that the procedure described above is — from CFD point of view — equivalent to forcing of the system. The base Ritz matrix is most often calculated as:

$$\mathbf{A}\,\mathbf{\Theta}^{(n)} = \mathbf{R}^{(n-1)} \tag{24}$$

where n is a number of the iteration. With a given initial set of $\mathbf{R}^{(0)}$, the set of $\mathbf{\Theta}^{(0)}$ vectors is found. The LU-decomposition of the $\mathbf{A}$ matrix can be done only once and several back-substitutions involving $\mathbf{R}$ vectors are quite effective, but requirements of storage for the decomposed matrix is rising dramatically with the number of degrees of freedom. In this work, the penalty method with the Finite Element Method and effective Quasi-Minimal-Residual Lanczos solver was adopted. We re-use the incomplete LU (ILU) decomposed matrix in each step. ILU decomposition is a compromise between the efficiency of back-substitution and memory limitations. To increase the numerical stability, the $\mathbf{\Theta}^{(i)}$ vectors are normalized after each step. The matrices for the reduced problem are calculated according to:

$$\begin{aligned} \hat{\mathbf{A}}^{(n)} &= \mathbf{\Theta}^{(n)^T}\,\mathbf{A}\,\mathbf{\Theta}^{(n)} = \mathbf{\Theta}^{(n)^T}\,\mathbf{R}^{(n-1)} \\ \hat{\mathbf{B}}^{(n)} &= \mathbf{\Theta}^{(n)^T}\,\mathbf{B}\,\mathbf{\Theta}^{(n)}. \end{aligned} \tag{25}$$

The matrix $\mathbf{\Theta}^{(n)}$ multiplication with matrices $\mathbf{A}, \mathbf{B}$ and the right-hand side reduces the eigenvalue problem to a smaller one. Matrices $\hat{\mathbf{A}}^{(n)}$ and $\hat{\mathbf{B}}^{(n)}$ have the assumed range of m. The value of m has to be a compromise between the computational resources as the eigenvalues for generalized eigenvalue problem for the $m \times m$ matrices has to be solved and the accuracy of the adequate representation of the physical problem.

The reduced generalized eigenvalue problem can be written as:

$$\left(\hat{\mathbf{A}}^{(n)} - \hat{\mathbf{\Omega}}^{(n)}\,\hat{\mathbf{B}}^{(n)}\right)\hat{\varphi^{(n)}} = 0. \tag{26}$$

Here, $\hat{\mathbf{\Omega}}$ is a diagonal matrix containing the eigenvalues of the reduced problem. This eigenvalue problem can be easily solved using any existing library algorithm. The eigenvectors for n-th iteration can be recalculated from the equation:

$$\varphi^{(n)} = {\mathbf{\Theta}^{(n)}}^T\,\hat{\varphi}^{(n)}. \tag{27}$$

If the convergence is not obtained, the new set of vectors $\mathbf{R}^{(n)}$ is calculated from

$$\mathbf{R}^{(n)} = \mathbf{B}\,\varphi^{(n)} \tag{28}$$

and the iteration has to be repeated.

4.3 Preconditioning

In the subspace iteration process, the subspace $span\left[\mathbf{\Theta}_1^{(k)}, \mathbf{\Theta}_2^{(k)}, \ldots \mathbf{\Theta}_m^{(k)}\right]$ tends to the subspace spanned by the eigenvectors corresponding to the eigenvalues having the smallest modulus. This is the so-called dominant subspace of the problem (19). The computed eigenpairs $(\lambda_i^k, \mathbf{x}_i^k), i = 1, \ldots m$ approximate the dominant eigensolution of the problem (19). The larger the difference (in sense of modulus) between the computed eigenvalues, the better is the convergence of the process. Because of this, we calculate more (m) to increase the convergence, even if we need only one eigenvalue. The convergence ratio is different for different eigenvalues To speed up the iteration we have to transform the rightmost eigenvalues into the dominant ones. For symmetrical eigenvalue problem already the real shift α is very effective if we know that α approximates the eigenvalue μ:

$$(\mathbf{A} - \alpha\mathbf{B})\mathbf{x} - \mu\mathbf{B}\mathbf{x} = 0. \tag{29}$$

In the case of the unsymmetrical eigenvalue problem, the eigenvalues are complex. This forces us to use a complex shift. However, a complex shift leads to complex matrices and thus increases significantly the computational costs. In order to avoid this complication, the inverse Cayley transformation

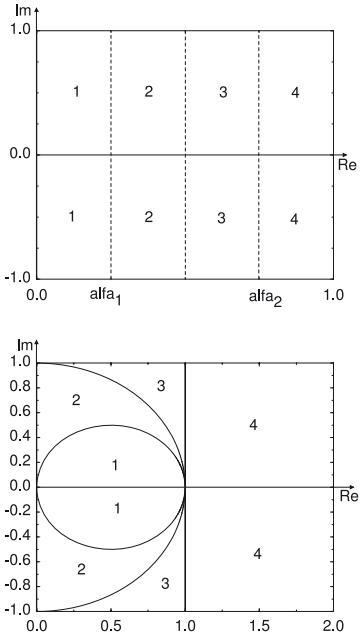

Figure 2. Spectrum mapping before (top) and after (bottom) the inverse Cayley transformation

with the real shift can be applied. Fig. 2 explains the transformation. The transformation of the problem (19) with the Cayley method results in:

$$((1-\alpha_3)\mathbf{A} - (\alpha_1 - \alpha_2\alpha_3)\mathbf{B})\mathbf{x} - \mu(\mathbf{A} - \alpha_2\mathbf{B})\mathbf{x} = 0. \tag{30}$$

The eigenvalues of the base problem (19) can be recalculated from the eigenvalues of (30) via the following formula:

$$\lambda = (\alpha_2(\mu + \alpha_3) - \alpha_1)/(\mu + \alpha_3 - 1). \tag{31}$$

The parameters $\alpha_1, \alpha_2, \alpha_3$ are real and enable us to deal only with the real system of equations. The uninteresting eigenvalues can be removed by manipulation of the subspace dimension and appropriate choice of shift parameters. The convergence rate can be significantly increased with the α_3 shift (α_3 has the same meaning as α in (29)). The rule is to set α_3 so that the modulus of the leftmost eigenvalue is smaller than all remaining eigenvalue moduli.

4.4 Eigensolution via system identification

The procedure based on snapshots starts with formulation of Hankel matrix (32), also called trajectory matrix:

$$\begin{bmatrix} u_0 & u_1 & \cdots & u_n \\ u_1 & u_2 & \cdots & u_{n+1} \\ \vdots & \vdots & \ddots & \vdots \\ u_n & u_{n+1} & \cdots & u_{2n-1} \end{bmatrix} = \begin{bmatrix} \tilde{u}_{11} & \tilde{u}_{12} & \cdots & \tilde{u}_{1n} \\ \tilde{u}_{21} & \tilde{u}_{22} & \cdots & \tilde{u}_{2n} \\ \vdots & \vdots & \ddots & \vdots \\ \tilde{u}_{n1} & \tilde{u}_{n2} & \cdots & \tilde{u}_{nn} \end{bmatrix} \begin{bmatrix} e^{\lambda_1 t_1} & e^{\lambda_1 t_2} & \cdots & e^{\lambda_1 t_n} \\ e^{\lambda_2 t_1} & e^{\lambda_2 t_2} & \cdots & e^{\lambda_2 t_n} \\ \vdots & \vdots & \ddots & \vdots \\ e^{\lambda_n t_1} & e^{\lambda_n t_2} & \cdots & e^{\lambda_n t_n} \end{bmatrix}. \quad (32)$$

It consists of values characterizing the flow, e.g. velocity, shifted by one position for subsequent time steps. The elements of Hankel matrix can be vectors consisting of values in a 'window' (block) over the flow.

The second matrix in (32) can be simplified assuming that $t_1 = 0$, having in mind that $t_n = t_1 + (n-1)\Delta t$ and denoting $\Lambda_n = e^{\lambda_n n \Delta t}$:

$$\begin{bmatrix} 1 & \Lambda_1 & \cdots & {\Lambda_1}^{n-1} \\ 1 & \Lambda_2 & \cdots & {\Lambda_2}^{n-1} \\ \vdots & \vdots & \ddots & \vdots \\ 1 & \Lambda_n & \cdots & {\Lambda_n}^{n-1} \end{bmatrix}. \quad (33)$$

This is called Vandermonde matrix. Now we construct another Hankel matrix, starting from the snapshot at $t = t_1 + \Delta t$. If we write the equation (32) in the form:

$$\mathbf{u} = \tilde{\mathbf{u}} e^{\lambda t}, \quad (34)$$

the new equation will have the form:

$$\mathbf{u}_{t+1} = \tilde{\mathbf{u}} \mathbf{\Lambda} e^{\lambda t}. \quad (35)$$

The shift to the left is equivalent to adding Δt to the exponents in (32), or, equivalently, the multiplication of the Vandermonde matrix with the diagonal matrix:

$$\begin{bmatrix} \Lambda_1 & 0 & \cdots & 0 \\ 0 & \Lambda_2 & \cdots & 0 \\ \vdots & \vdots & \ddots & \vdots \\ 0 & 0 & \cdots & \Lambda_n \end{bmatrix}. \quad (36)$$

With equations (34) and (35), the eigenvalue problem can be re-stated:

$$\mathbf{A}\tilde{\mathbf{u}} = \tilde{\mathbf{u}}\mathbf{\Lambda} \quad \text{with} \quad \mathbf{A} = \mathbf{u}_{t+1}\mathbf{u}^{-1}. \tag{37}$$

The $\mathbf{A}$ matrix can be also formulated in a more complex way employing $\mathbf{u}_{t+1}, \mathbf{u}_{t+2}$ etc. Important factors are, however, not the formulation but the eigensolutions of the (37). The mentioned similarity to POD approach would suggest the Singular Value Decomposition (SVD) method. The algorithm of SVD, which consists mainly of the eigensolver, could be potentially used also in this case. The $\mathbf{A}$ matrix is now real but non-Hermitian. Hence, a complex procedure has to be applied and complex eigenvalues and eigenvectors are the result, as in case of eigenproblem resulting from linearized Navier–Stokes equations (§ 4.1). In the form (37) the matrix is large but we can apply reduction of the large-dimensional space similarly to methods applied in § 4.1. We can also formulate the trajectory matrix for the part of the domain- 'window' only. There are also more serious numerical challenges. $\mathbf{A}$ matrix is a product of weighting $\mathbf{u}_{t+1}\mathbf{u}^{-1}$ and forms a companion matrix, with only one non-zero column and unit values below main diagonal:

$$C(p) = \begin{bmatrix} 0 & 0 & \dots & 0 & -c_0 \\ 1 & 0 & \dots & 0 & -c_1 \\ 0 & 1 & \dots & 0 & -c_2 \\ \vdots & \vdots & \vdots & \vdots & \vdots \\ 0 & 0 & \dots & 1 & -c_{n-1} \end{bmatrix}. \tag{38}$$

Performing the SVD on the product may introduce catastrophic roundoff errors. In case of wide range of singular values of both matrices, the small singular values of the product can be either not computed accurately or not found at all. To compute the SVD of (37) $\mathbf{A}\mathbf{B}^{-1} = \mathbf{U}\mathbf{\Sigma}\mathbf{V}^*$, two decompositions of $\mathbf{A}$ and $\mathbf{B}$ are performed: $\mathbf{A} = \mathbf{U}\mathbf{\Sigma}_A\mathbf{X}$ and $\mathbf{B} = \mathbf{V}\mathbf{\Sigma}_B\mathbf{X}$. The generalized singular values of $\mathbf{A}$ and $\mathbf{B}$ are computed with diagonal matrices $\mathbf{\Sigma} = \mathbf{\Sigma}_A\mathbf{\Sigma}_B^{-1}$. The keywords for solution of the problem (37) is PSVD (for Product SVD), QSVD (for Quotient SVD). The details of the algorithms are provided in numerous papers of G.H. Golub.

5 Stability results for the cylinder wake

5.1 Steady flow global stability

A solution of the eigenvalue problem (19) consists of the leading eigenvalues depicted in Fig. 3 and eigenvectors shown in Fig. 7. The eigenvalues are mostly complex with the real part being the growth rate and the imaginary part being the angular frequency, i.e. $2\pi \times St$ (St: Strouhal number).

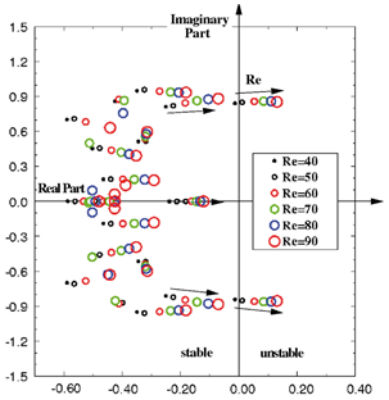

Figure 3. The eigenvalue spectrum for a circular cylinder flow and its change with the increasing Reynolds number

Complex eigenvalues are characteristic for oscillatory flow. Non-oscillatory modes, with the eigenvalues laying on the imaginary axis are characterized by vanishing frequency. The dominant non-oscillatory flow is typically related to base flow changes, and thus to the shift mode explained later. With increasing Reynolds number, the flow becomes unstable, i.e. the leading eigenvalue moves from the left into the right-half plane of Fig. 3. For wake behind a circular cylinder, the critical Reynolds number is about $Re_c = 47$. At larger (smaller) Reynolds numbers any disturbance present in the flow is amplified (decaying).

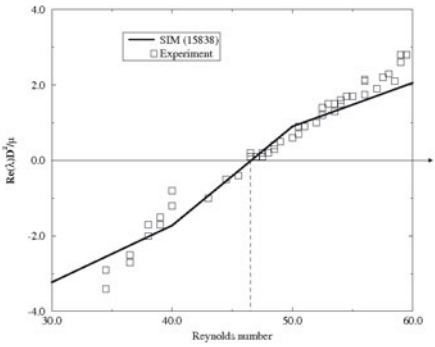

Figure 4. Comparison of the disturbance growth-rate obtained in computation (SIM) and experiment (Schumm, 1991)

The critical Reynolds number determined by the global stability analy-

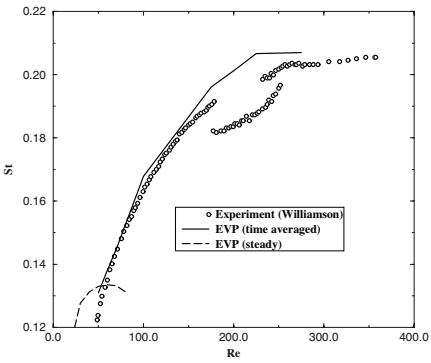

Figure 5. Strouhal number of circular cylinder flow obtained with the stability analysis of the steady flow and of the averaged solution. In addition, experimental values for periodic vortex shedding are shown.

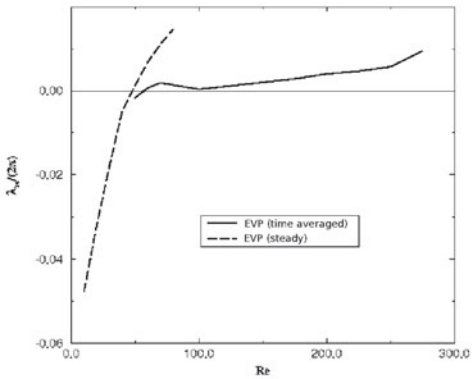

Figure 6. Comparison of the growth-rate based on the steady solution and averaged periodic one.

sis compare (Tab. 1) is in very good agreement with the experiment. Also the growth rate, Fig. 4, agrees with the experimental values by Schumm (Schumm, 1991) in the neighborhood of the critical Reynolds number. The values of the Strouhal number and growth rate deviate from the experiment as the Reynolds number increases above the critical value as shown in Figs. 5 and 6. The Strouhal number at larger Reynolds numbers is unphysically decreasing, while the growth rate is monotonically increasing, even for Reynolds number higher than the critical one. This feature is the consequence of linearization of our flow model.

The eigenanalysis of the flow is targeting the determination of the physical modes — as opposed to numerical ones. The leading complex eigenvector

Table 1. Critical values for circular cylinder flow

Critical value	Re_c	St_c
Jackson (Jackson, 1987)	45.4	0.1363
Zebib (Zebib, 1987)	$39 - 43$	$0.11 - 0.13$
Strykowski (Strykowski and Sreenivasan, 1990)	46.0	-
Schumm (Schumm, 1991)	46.6	
global stability analysis	47.00	0.1320

relates to von Kármán vortex shedding for the flow around circular cylinder and is shown in Fig. 7 at various Reynolds numbers. The eigenvector patterns of Fig. 7 are similar for a large class of wake flows. The modes can be determined even for stable flows at small Reynolds numbers. At larger Reynolds number, the maximum intensity of disturbance energy is moving toward the cylinder. The disturbance structures are getting smaller as the wavenumber increases with the flow Reynolds number. Fig. 8 depicts the result of the computation for much larger computational domain ($x = 45D$) and $Re = 100$. It shows the streamlines in the domain, with maximum intensity of the fluctuation behind the cylinder and decaying in the direction of the outflow. Fig. 8 confirms that computations depicted in Fig. 7 are not significantly effected by the far–field boundary conditions at $x = 15$.

5.2 Time–averaged flow stability

We observe that ROM with the stability eigenmodes can be accurate at the Reynolds numbers close to the critical one. See also the results presented in § 5. The results presented in § 7.4 for the airfoil corroborate that statement. The stability analysis of the mean flow is an interesting alternative to the one of the steady solution. One can expect that a linearization of the Navier-Stokes equation at the center of the flow attractor may, in some sense, be more accurate than at the steady solution, which is further away. The base flow has frequently been observed to be marginally stable corroborating a conjecture by Malkus (Malkus, 1956). Under mean-field assumptions, marginal stability of time–averaged (mean) flow was proven by Noack et al. (Noack et al., 2003). The plots in Fig. 5 and 6 showing that indeed the time–averaged flow has physically correct, nearly zero growth rate (is marginally stable). Moreover, the stability-inferred frequency approximates the true Strouhal number for the whole laminar Reynolds number

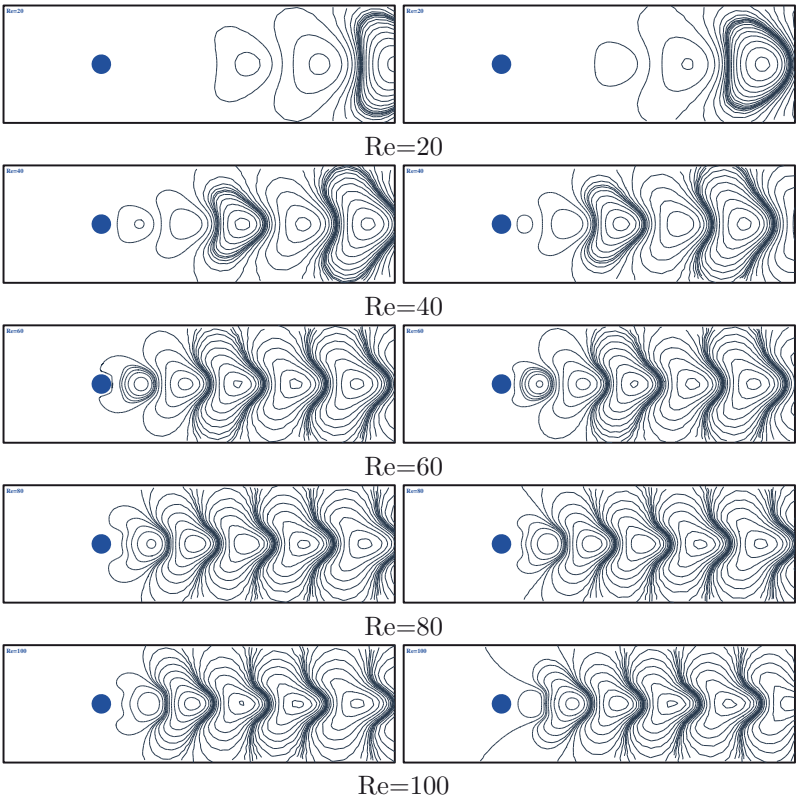

Figure 7. Leading complex eigenvector for the flow around a circular cylinder at Re = 20, 40, 60, 80 and 100 from top to bottom, respectively. The real (imaginary) part is shown in the left (right) column.

range. This was first presented in 1999 in (Morzyński et al., 1999a). Also the eigenmodes of time–averaged flow are more 'POD–like' (Fig. 9), suggesting that these modes can be a better alternative than the classical, steady flow based ones at supercritical Reynolds numbers. The theory and results are not presented here, the results in (Morzyński et al., 2006a) show the implementation of time–averaged eigenmodes in construction of the *a priori* flow model.

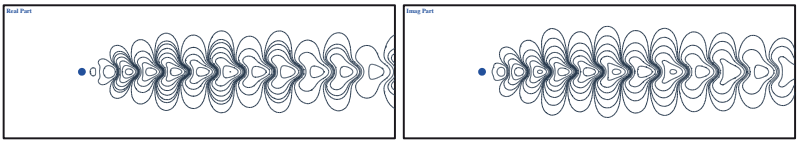

Figure 8. Same as Fig. 7 but at $Re = 100$ in larger computational domain.

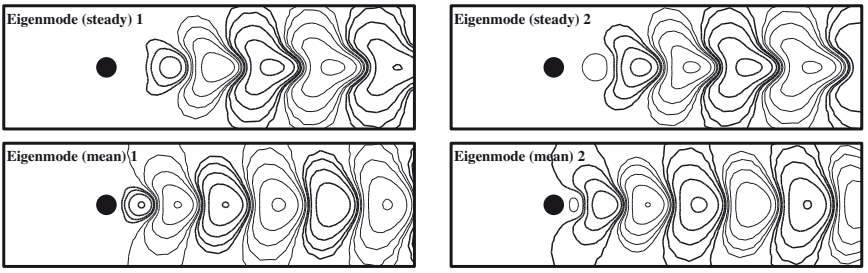

Figure 9. Flow around a circular cylinder at $Re = 100$. Streamlines of real (left) and imaginary (right) parts of the leading pair of eigenmodes for linearization around steady solution (top) and time-averaged one (bottom).

6 Wake control

6.1 General philosophy of flow control for stabilization

In the following, we show how flow control for stabilization can be guided by CFD and the global stability analysis presented earlier.

Any spatial discretization (FDM, FEM, FVM) of the linearized disturbance equation (2) yields a finite-dimensional evolution equation of the form

$$\frac{d}{dt}\,\mathbf{a} = \mathbf{A}\,\mathbf{a}, \tag{39}$$

where $\mathbf{a}$ is a vector of state variables. State variables are dependent on the formulation, for instance, the velocity components at the grid nodes, stream function, stream function and vorticity.

The matrix $\mathbf{A}$ has a natural spectrum of eigenvalues similar to depicted in Fig. 10. A conjugate pair of eigenvalues laying in the right-hand side of the imaginary axes of the complex plane represent the flow instability. Flow control techniques are targeting suppression of the instability.[1]

[1] Enhancement of instability for instance to increase mixing is also possible but not in the scope of this chapter.

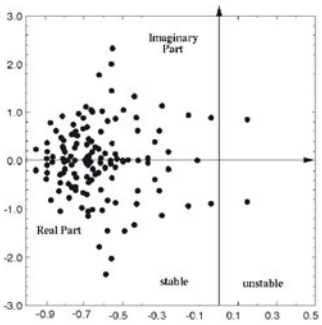

Figure 10. Stability spectrum of steady flow around a circular cylinder at $Re = 100$

Suppression of instability implies an actuator leading to a *small* change of matrix $\mathbf{A}$ which moves the unstable eigenvalues to the left-hand (stable) half of the complex plane. A general control approach can be expressed by adding to the Navier-Stokes equations a volume force term. This leads to a finite-dimensional evolution equation of the form

$$\frac{d}{dt}\,\mathbf{a} = \mathbf{A}\,\mathbf{a} + \mathbf{B}\,\mathbf{b}. \tag{40}$$

Here $\mathbf{b}$ represents a vector for the volume force amplitudes and the matrix $\mathbf{B}$ is the gain from the corresponding local force fields. The volume force $\mathbf{Bb}$ can substantially change the solution of the Navier-Stokes equations. It can mimic active or passive control devices. An active proportional controller $\mathbf{b} = -\mathbf{K}\,\mathbf{a}$, for instance, gives rise to the forced dynamics

$$\frac{d}{dt}\,\mathbf{a} = \mathbf{A}^c\mathbf{a}, \tag{41}$$

with the modified linear term $\mathbf{A}^c = \mathbf{A} - \mathbf{B}\,\mathbf{K}$. Here, the design parameter $\mathbf{K}$ may be used to stabilize or destabilize the system. With this assumption, (41) has the same form as (39) and the control goal becomes once more the desired manipulation of the eigenvalue spectrum of a matrix.

Besides volume forces, also models with wall-mounted actuators can be written in the form (40) (Rediniotis et al., 2002).

In the penalty method of CFD, obstacles are modeled by time-dependent volume forces which lead to vanishing velocity inside the obstacle. This corresponds to a local actuation term $\mathbf{Bb}$ and a strongly stabilizing controller $\mathbf{b} = -\mathbf{K}\mathbf{a}$. Thus, the actuation term of (41) may model passive control with control wires, splitter plates, riblets or other devices. Here, $\mathbf{A}^c$ describes the effect of the device and optimization of a passive device may be guided by global stability analysis. An example is provided in § 6.2.

6.2 Wake stabilization using model-based passive control

(a) (b)

Figure 11. Real (a) and imaginary (b) part of the most unstable eigenmode of the passively manipulated cylinder wake at $Re = 100$. The control cylinder ($d/D = 0.1$) is placed at $x = 1.2, y = 1.2$. The cylinder is indicated by the solid circle and the flow field is visualized with streamlines. Thick (thin) lines correspond to positive (negative) stream-function values.

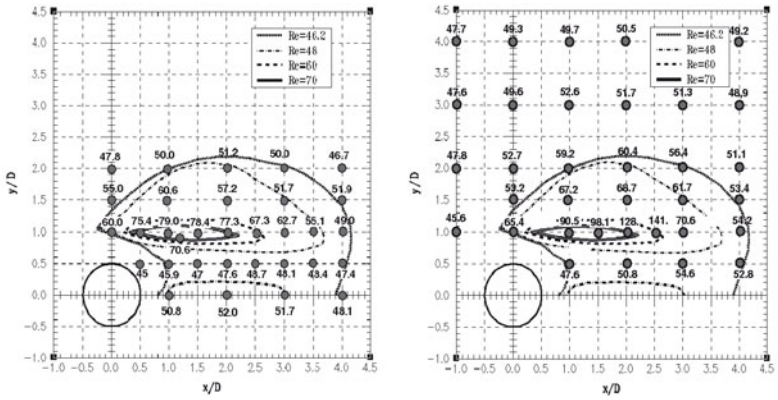

(a) One control cylinder (b) Two control cylinders

Figure 12. Optimization of passive control with one and two Strykowski wires employing global flow stability analysis. The dots and numbers in the field denote the control cylinder position and respective critical Reynolds numbers. The second control cylinder in subfigure (b) is placed symmetrically with respect to the x-axis.

Passive suppression of vortex shedding may be achieved with splitter plates (Unal and Rockwell, 1987; Mittal, 2003) or small control cylinders

(Strykowski and Sreenivasan, 1990). In this case, the $\mathbf{A}^c$ matrix of (41) is computed in terms of parameters of passive actuators. The no-slip conditions on the surface of a control cylinder or a splitter plate can be imposed with a penalization of the surface velocities with time- and space-dependent volume forces. Thus, we can study how the geometry of passive actuators is related to the flow stability varying the parameters of the actuator (like position or size). In this way, the linear model can be employed to optimize passive control. This approach is demonstrated for the Strykowski control cylinder (Strykowski and Sreenivasan, 1990). The critical Reynolds number is determined at different locations of the control cylinder with global nonparallel flow stability analysis (Fig. 11). The eigenanalysis (see Fig. 12) yields the optimal position for one and two symmetrically placed control cylinders. Isolines in that figure denote the critical Reynolds number values found experimentally in (Strykowski and Sreenivasan, 1990), small circles denote analyzed positions of the control cylinder, and the numbers represent critical values obtained by global stability analysis.

The critical Reynolds number is largest for control wire positions in a narrow shear-layer region behind the cylinder. Global stability analysis predicts also that any non-symmetrical configuration is less effective for stabilization than the optimal symmetrical one.

The passive control optimization with Strykowski wires depicted in Fig. 12 shows good agreement with experiment. Below the position-dependent critical Reynolds number, the steady solution is at least locally stable. The agreement of the largest achievable critical Reynolds number in experiment and in the current study suggests the domain of attraction of the steady solution contains at least the periodic shedding state and may even contain all flows. We can also extend the investigation and solve the *sensitivity* problem for the flow to determine the regions most sensitive to passive actuation. Technically, one has to solve the adjoint eigenvalue problem (Giannetti and Luchini, 2007) with similar techniques as used for the regular one (19).

7 Weakly non-linear models

7.1 Mean-field correction

We can use real and imaginary part of the eigenvector to build a Galerkin model of the flow. For the flow around a circular cylinder, the initial growth rate $\sigma = 0.1439$ and Strouhal number $St = 0.1346$ are in good agreement with the simulation. Apart from exponential divergence of the Galerkin solution, the stability modes can resolve only about 41% of the turbulent kinetic energy of the periodic vortex shedding. The reason is the changing

structure of vortex shedding at the limit cycle. The maximum fluctuation level moves from far downstream, as predicted by the stability modes, to close to the cylinder, as resolved by the first POD modes.

The alternative, a ROM obtained with the POD Galerkin method (see chapter of B.R. Noack et al.) is highly efficient and resolves nearly perfectly the kinematics of the flow. At the same time, it is highly fragile and sensitive to changes in the parameters or operating conditions. For the circular cylinder wake, the first two POD modes capture about 95% of the fluctuation energy. Yet, a Galerkin model (GM) based on these two modes alone is unstable for physical reasons. The inclusion of eight POD modes, capturing the first four harmonics of the attractor, suffices to achieve nearly perfect resolution and weakly stable Galerkin model. Yet, the correct prediction of the system dynamics with this model is limited to a small neighborhood of the attractor and to relatively small Reynolds number changes. In particular, the oscillatory dynamics associated with linear instability from the steady solution is not well resolved. Further increase in number of POD modes does not cure the problem and violates the targeted low dimensionality of the model. Hence, we have to find other ways of stabilization.

Stabilization of the GM can be obtained with the shift mode (Noack et al., 2003) as suggested by the mean-field theory. The shift mode is a normalized difference $\mathbf{u}_0 - \mathbf{u}_s$ where $\mathbf{u}_0$ is mean flow solution and $\mathbf{u}_s$ is (unstable) steady solution. Figure 13 illustrates the concept. The vertical axis is referring to the base flow state. The radius of the paraboloid is the amplitude of the fluctuation for natural transient between instability and the limit cycle at the top of the paraboloid. The bottom fixed point on the paraboloid represents the unstable steady flow solution shown at the left part of the figure. Fluctuations at this point are well approximated by the stability eigenmodes. One of the modes is shown at the right part of the figure. The center of the limit cycle corresponds the the mean flow (left) with associated POD modes (right). The difference between the steady flow solution and the mean flow of the limit cycle is characterized by the length of the recirculation bubble. Evidently, this base flow change cannot be resolved by the oscillatory eigenmodes obtained with global stability analysis.

For robustness, we have to add to the Galerkin system the missing direction, connecting both states of the flow. It is the shift mode depicted in the middle of the figure. The inclusion of the shift mode reduces significantly the model sensitivity to parameter variations.

Up to now, we only defined the kinematic shift mode and pointed out its importance for flow modeling. In (Tadmor et al., 2010), the dynamic role of mean-field variations and transient energy flow analysis is presented. It is proven that the shift mode is indispensable to represent that contri-

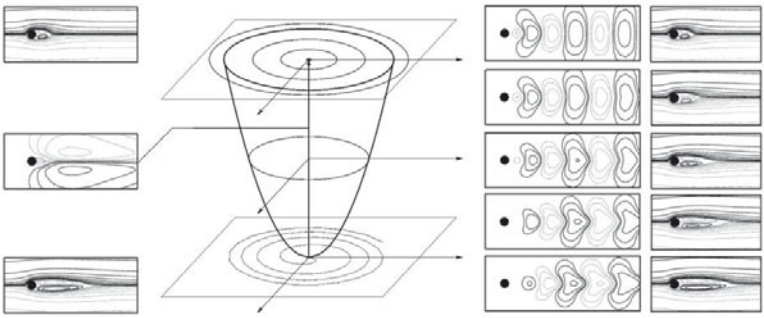

Figure 13. Principal sketch of the transient wake dynamics. The left side displays the mean flow (top), shift-mode (middle) and steady solution (bottom). The right side illustrates interpolated modes and vortex streets on the mean-field paraboloid. The flow fields are depicted as the streamline plots.

bution. The shift mode can be computed with many methods as presented in (Tadmor et al., 2010). We show only the shift mode derived from the Reynolds-Averaged Navier-Stokes (RANS) equation:

$$\bar{u}_j \bar{u}_{i,j} + \bar{p}_{,i} - \frac{1}{Re} \bar{u}_{i,jj} + (\overline{\acute{u}_j \acute{u}_i})_{,j} = 0. \tag{42}$$

The Reynolds stress term is well approximated by:

$$(\overline{\acute{u}_j \acute{u}_i})_{,j} = \mathcal{K} \nabla \cdot (\tilde{\mathbf{u}}_1 \otimes \tilde{\mathbf{u}}_1 + \tilde{\mathbf{u}}_2 \otimes \tilde{\mathbf{u}}_2)\,, \tag{43}$$

where $\mathcal{K}(t)$ is the mean fluctuation energy averaged over one period T, and $\tilde{\mathbf{u}}_{1,2}$ is the dominant POD mode pair.

Figure 14 shows the kinematic and an *a priori* shift mode computed with (42), in virtually good agreement. It may be worthwhile to note that higher-order modes can be derived from the non-linear Navier-Stokes term and utilizing harmonic expansions (Dušek et al., 1994), considering each POD mode pair as one harmonic. Hence, refined *a priori* models are in reach, too.

The dynamics of the least-order (3-dimensional) Galerkin model enriched with a shift mode is compared with a DNS in Fig. 15. The shift mode is the the first step and the key enabler for construction of transient, control-oriented models. This subject will be elaborated in the chapter by G. Tadmor et al. The reader should refer for more details there.

Figure 14. Empirical (left) and a priori (right) shift mode. The empirical mode is computed from the mean flow and steady solution as described in (Noack et al., 2003). The a priori shift mode is derived from the Reynolds equation using the POD representation of the Reynolds stress tensor.

7.2 Hybrid model employing stability modes

Further improvement of the model dynamics can be obtained with a hybrid model employing POD *and* stability modes (Morzyński et al., 1999b). In this model, POD resolves the attractor and stability eigenmodes resolve the linearized dynamics. Thus, dynamic transient and post-transient flow behavior is accurately predicted. The concept of hybrid model reduces significantly the number of necessary degrees of freedom of the system in comparison to the purely POD-based one. The hybrid approach is demonstrated for benchmark problem of the flow around circular cylinder in (Noack et al., 2003). The transients of the hybrid models are compared with DNS in Fig. 15. The hybrid model combines the advantages of both reduced models. It converges to the limit cycle preserving initially the growth rate predicted by global stability analysis.

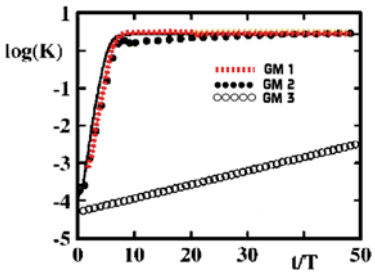

Figure 15. Transients of various Galerkin models. The logarithm of the fluctuation energy over time nondimensionalized with the period T. Galerkin model: GM 1 - with shift mode and 2 interpolated modes, GM 2 - as GM 3 with shift mode and leading stability mode added, GM 3 - with 8 POD modes.

7.3 Continuous mode interpolation

Additive interpolation procedures, based on the superposition of two modes ensembles like the one described in section § 7.2 may resolve different operating conditions. For model–based control the modes need to be additionally 'flexible' and smoothly change at different operating conditions (Luchtenburg et al., 2006)(Siegel et al., 2006). Let us consider the interpolation problem of periodic cylinder wakes at two operating conditions. The resulting vortex streets look similar but may have slightly different wavenumbers, frequencies, and fluctuation envelopes. The states may, for instance, be near the onset of vortex shedding and the asymptotic state (Noack et al., 2003)(Siegel et al., 2006). Other pairs of states are the natural and forced wake (Luchtenburg et al., 2006), or the natural flow at two different Reynolds number (Deane et al., 1991). We are looking for a method which smoothly interpolates the modes of different states in the way shown schematically in Fig. 16. The straightforward idea of 'morphing' used in image processing could be an inspiration but we shall use here a more advanced method and interpolate the discrete operators for different operating conditions, to generate the modes for a continuum of intermediate states.

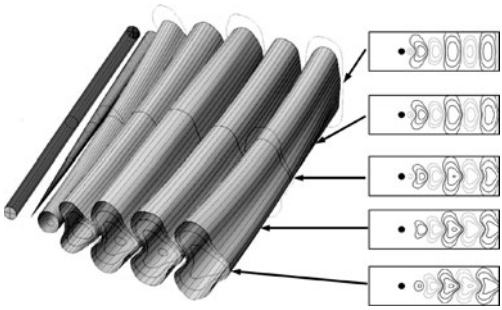

Figure 16. Principal sketch of continuous mode interpolation. Left: Transition between stability eigenmodes and POD modes. Right: streamlines of the intermediate states

In the following, we outline a continuous interpolation technique which will yield modes with all intermediate wavenumbers and frequencies.

For example, the most amplified stability eigenmodes of the linearized Navier-Stokes equation at two base flows can be interpolated. We assume one dominant oscillatory eigenmode, like for the flow around a bluff cylinder (Morzyński et al., 1999b). Then, the associated two sets of modes constitute complex eigenmodes $\mathbf{f}^\kappa = \mathbf{u}_1^\kappa + \imath \mathbf{u}_2^\kappa$ of the eigenvalue problem

$$\mathbf{A}^\kappa \, \mathbf{f}^\kappa = \lambda^\kappa \, \mathbf{f}^\kappa, \quad \kappa = 0, 1, \tag{44}$$

where λ^κ are the associated eigenvalues. Here, $\mathbf{A}^\kappa$ is the linearized FEM

discretization of the Navier-Stokes operator forming the stability matrix. The stability matrix may be linearly interpolated for $\kappa \in [0, 1]$,

$$\mathbf{A}^{\kappa} = \mathbf{A}^{0} + \kappa\,(\mathbf{A}^{1} - \mathbf{A}^{0}), \tag{45}$$

thus giving rise the intermediate eigenproblems of the form (44) and intermediate complex eigenmodes $\mathbf{f}^{\kappa} = \mathbf{u}_1^{\kappa} + \imath\mathbf{u}_2^{\kappa}$. A smooth connection between both eigenmodes is not guaranteed per se but can be expected for the most unstable stability modes of shear flows.

The example presented here represents the simplest case of continuous mode interpolation. More advanced problems of interpolation of stability and POD bases, characterized by matrices of different size, mode extrapolation to new operating conditions or building of *a priori* flow models with stability eigenmodes are described in (Morzyński et al., 2006a) and (Morzyński et al., 2006b).

7.4 Mean field correction and Galerkin Model for NACA-0012 flow

We aim at designing a flow model for feedback flow control. Low-dimensionality and simplicity is required for the online-capable feedback laws. Robustness of flow control models implies even stronger limitations on 'superfluous' degrees of freedom. A frequent observation is that observers and controllers derived from higher-fidelity models are less robust.

A low-dimensional representation of the natural flow should be the first test of such a model. We first construct a ROM using the Galerkin method, presented in the chapter of B.R. Noack et al. in this volume. As mode basis, we can use POD and stability eigenmodes. We apply the technique of continuous mode interpolation to connect both types of modes smoothly.

We continue our ROM flow consideration for the example of a flow around a NACA-0012 airfoil having the angle of attack of 30 degrees. This typical wake flow can be treated as representative for 'real life' one, for which we intend to build the Galerkin model. With standard procedure, described in § 4 we determine the base flow, Fig. 17, and eigenmodes of the steady and time-averaged solutions, Fig. 18.

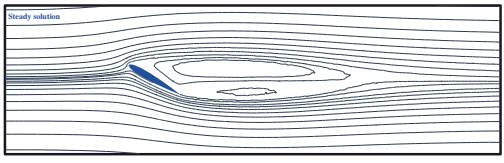

Figure 17. Flow around NACA-0012 airfoil - streamlines of the steady solution.

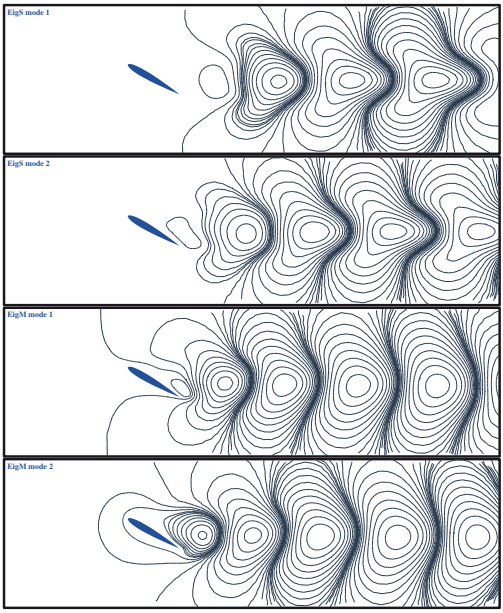

Figure 18. The most dominant eigenmodes pairs based on the steady solution (top two figures, $\lambda = -0.147 \pm 0.720\imath$) and time-averaged solution (bottom two figures, $\lambda = 0.018 \pm 0.915\imath$)

We also compute the first four POD modes with the snapshot POD method (Sirovich, 1987). (Fig. 19).

With the determined mode basis and POD Galerkin method, we construct the Galerkin model of the flow. The conclusions from this numerical experiment can be expected to representative for all Galerkin models of the wake flow. In Fig. 21, the shift-mode amplitude is shown as a function of fluctuation amplitude, both, for the Galerkin model and for the DNS. The deviation of the curves from the values for DNS is a measure of the model quality.

The first observation is that for all presented models, we have to employ the mean-field correction (shift mode) to avoid the structural instability and thus fragility of the ROM.

It can be seen in Fig. 21 that POD modes allow the reconstruction of Navier-Stokes attractor (limit cycle), but they are unable to reproduce the dynamical properties of transitional flow. For the flow states close to fixed point (steady solution, small values of shift-mode coefficient), the kinetic energy of the flow is overestimated — especially in POD-2 Galerkin model.

The models based on the two most unstable eigenmodes (Fig. 20, middle) reconstruct the flow states close to fixed-point (steady solution) and the

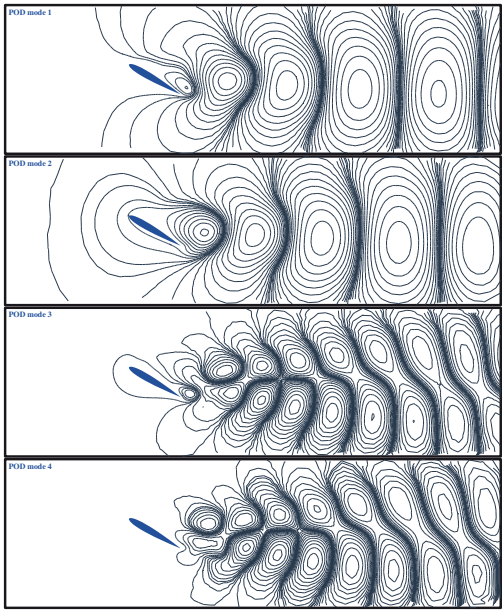

Figure 19. First 4 POD modes for the NACA-0012 airfoil flow

transition to limit cycle better than POD Galerkin models. On the other hand the limit-cycle disturbance kinetic energy and shift-mode coefficients of periodic flow are significantly underestimated with these mode bases.

The last of the models presented here is the least-dimensional model of continuous interpolated mode pair using the technique described in section § 7.3.

The comparison shows that dynamical properties of simple ROMs can be unsatisfactory. At the same time, special techniques allows construction of least–dimensional model having very good dynamical properties. This study demonstrates that not only the appropriate expansion mode basis but also modeling skills are a necessary ingredient in ROM design.

8 Summary and perspectives - 3D flow stability analysis

We have presented the foundations of global flow stability analysis and its role in fluid dynamics. An interested reader should be able to adapt his own numerical code or any of the open source ones to compute the global stability eigensolutions and use the results for ROM modeling, possibly employing

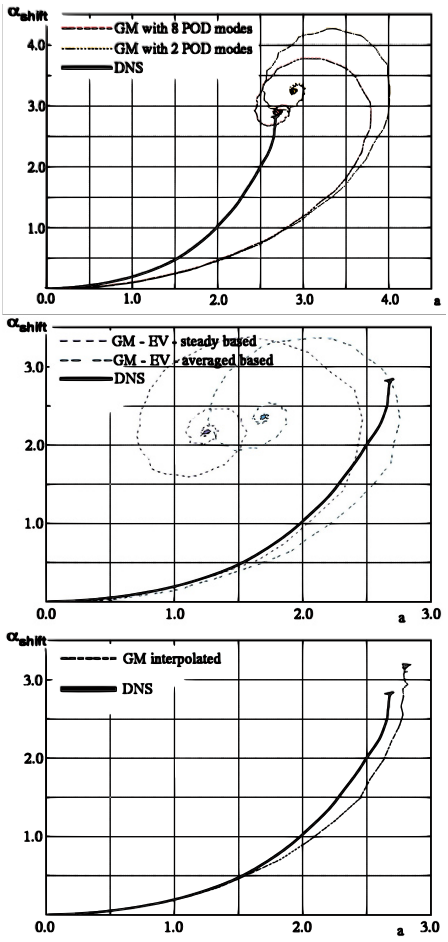

Figure 20. Shift-mode amplitude as a function of fluctuation amplitude for POD-based models (top), eigenmode-based models (middle), and interpolated model (bottom). The solid black line corresponds to the CFD benchmark.

further detailed descriptions.

The global stability analysis begun in late 80's of the last century. Recent interest in feed-back control using ROM enhanced also investigations in this direction. Stability modes are characterized by a single frequency for each mode pair and may thus constitute a 'clean' piano with 'pure tones'. By construction, stability modes are the optimal mode basis for modeling the transients near the onset of instability. As alternative, Galerkin expansion piano may be build from POD modes of given solutions. By construction, POD resolves the energy of the fluctuation in optimal way but may mix

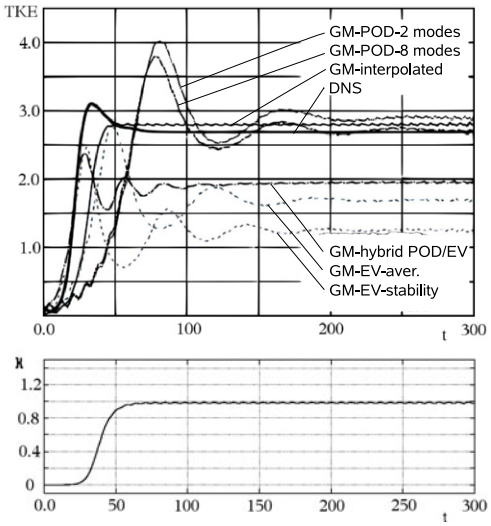

Figure 21. The variation of disturbance kinetic energy (TKE) for different Galerkin models and interpolation parameter κ as a function of time. The flow transitions from steady state to the limit cycle oscillation. The displayed Galerkin model can be inferred from the legend.

several frequencies in a single mode (Rowley et al., 2009). Combination of the POD mode basis with stability modes is shown to improve the ROM dynamics. In a more refined approach, the evolution of stability eigenmodes towards POD modes is parameterized by a continuous mode interpolation, thus removing unnecessary degrees of freedom in the modal expansion. In this case, the interpolation employs also a solution of the eigenvalue problem.

The computational aspects of the eigensolution computation has been explained in detail. The formulation of the problem was presented for 2D and 3D case. We interpreted the eigenvalue solution procedure from the point of view of CFD methods, speaking in terms of practical numerics. Particularly noteworthy is the similarity between state space reduction for solution of the eigenvalue problem and other methods employed in model reduction. The computational methods of global flow stability analysis have benefitted from recent developments in global flow stability from physical methods employed for ROMs, from signal processing, from system identification and from CFD.

The computational challenges of 2D global flow stability are now trivial in comparison with problems of early development of the method. At the same time, the 3D global flow stability is still a challenge, no matter what method is used for eigensolution. In Figs. 22 and 23 we show that also for 3D geometry it is possible to extract eigenmodes with the described method.

The solution of these computational problems are a key enabler for ROMs of 3D flows of practical importance. Other methods, as described in this chapter and in this book can be expected to serve as further catalyzers.

Figure 22. Left: Unstructured, 3D computational grid with partitioning for parallel computation; Right: Steady flow solution for the 3D flow around the sphere - zero velocity isosurface is shown for $Re = 300$.

Figure 23. Real parts of two higher eigenmodes for the 3D flow around the sphere at $Re = 300$. Isosurfaces indicate constant streamwise (V_x) velocity. The grayscale shows the positive and negative sign of the velocity.

Bibliography

E. Åkervik, J. Hœpffner, U. Ehrenstein, and D. S. Henningson. Optimal growth, model reduction and control in a separated boundary-layer flow using global eigenmodes. *J. Fluid Mechanics*, 579:305–314, 2007.

D. Amsallem and C. Farhat. Interpolation method for adapting reduced-order models and application to aeroelasticity. *AIAA Journal*, 46(7): 1803–1813, 2008.

S. Bagheri, D. S. Henningson, J. Hœpffner, and P. J. Schmid. Input-output analysis and control design applied to a linear model of spatially developing flows. *Applied Mechanics Reviews*, 62:020803, 2009.

A. J. Baker. *Finite Element Solution Algorithm for Viscous Incompressible Fluid Dynamics*. John Wiley and Sons, New York, 1983.

R. Becker, M. Garwon, C. Gutknecht, G. Bärwolff, and R. King. Regelung aerodynamischer Strömungen am Beispiel einer rückwärtsgewandten Stufe (transl.: Control of aerodynamics flows examplified for the backward-facing step). *Automatisierungstechnik*, 50:79–86, 2002.

M. Bergmann, L. Cordier, and J. P. Brancher. Optimal rotary control of the cylinder wake using proper orthogonal decomposition reduced order model. *Phys. Fluids*, 17:097101–097121, 2005.

T. J. Chung. *Computational Fluid Dynamics*. Cambridge University Press, Cambridge, U.K., 2002.

A. E. Deane, I. G. Kevrekidis, G. E. Karniadakis, and S. A. Orszag. Low-dimensional models for complex geometry flows: Application to grooved channels and circular cylinders. *Phys. Fluids A*, 3(10):2337–2354, 1991.

J. Dušek, P. Le Gal, and P. Fraunie. A numerical and theoretical study of the first Hopf bifurcation in a cylinder wake. *J. Fluid Mech.*, 264:59–80, 1994.

F. Giannetti and P. Luchini. Structural sensitivity of the first instability of the cylinder wake. *J. Fluid Mechanics*, 581:167–197, 2007.

C. P. Jackson. A finite-element study of the onset of vortex shedding in flow past variously shaped bodies. *J. Fluid Mech.*, 182:23–45, 1987.

B. H. Jørgensen, J. N. Sørensen, and M. Brøns. Low-dimensional modeling of a driven cavity flow with two free parameters. *Theoret. Comput. Fluid Dynamics*, 16:299–317, 2003.

A. I. Khibnik, S. Narayanan, C. A. Jacobson, and K. Lust. Analysis of low dimensional dynamics of flow separation. In *Continuation Methods in Fluid Dynamics. Notes on Numerical Fluid Mechanics, vol. 74*, pages 167–178. Vieweg, 2000. Proceedings of ERCOFTAC and Euromech Colloquium 383, Aussois, France, September 6–9, 1998.

T. Lieu, C. Farhat, and M. Lesoinne. Reduced-order fluid/structure modeling of a complete aircraft configuration. *Computer Meth. Appl. Mech. Engr.*, 195(41-43):5730–5742, 2006.

D. M. Luchtenburg, G. Tadmor, O. Lehmann, B. R. Noack, R. King, and M. Morzyński. Tuned POD Galerkin models for transient feedback regulation of the cylinder wake. In *44th AIAA Aerospace Sciences Meeting and Exhibit*, Reno, Nevada, USA, 2006. AIAA-Paper 2006-1407.

X. Ma and G. E. Karniadakis. A low-dimensional model for simulating three-dimensional cylinder flow. *J. Fluid Mech.*, 458:181–190, 2002.

W. V. R. Malkus. Outline of a theory of turbulent shear flow. *J. Fluid Mech.*, 1:521–539, 1956.

S. Mittal. Effect of a "slip" splitter plate on vortex shedding from a cylinder. *Phys. Fluids*, 9:817–820, 2003.

M. Morzyński, K. Afanasiev, M. Braza, and F. Thiele. Eigenmodes and empirical eigenmodes in flow stability and control. In *Proceedings IS-CFD'99, All Contributions*, 1999a. International Symposium Computional Fluid Dynamics, Bremen, 5-10 September 1999.

M. Morzyński, K. Afanasiev, and F. Thiele. Solution of the eigenvalue problems resulting from global non-parallel flow stability analysis. *Comput. Meth. Appl. Mech. Enrgrg.*, 169:161–176, 1999b.

M. Morzyński, W. Stankiewicz, B. R. Noack, R. King, F. Thiele, and G. Tadmor. Continuous mode interpolation for control-oriented models of fluid flow. In R. King, editor, *Active Flow Control*, pages 260–278. Springer–Verlag, 2006a.

M. Morzyński, W. Stankiewicz, B. R. Noack, F. Thiele, and G. Tadmor. Generalized mean-field model with continuous mode interpolation for flow control. In *3rd AIAA Flow Control Conference*, San Francisco, Ca, USA, 2006b. AIAA-Paper 2006-3488.

B. R. Noack, K. Afanasiev, M. Morzyński, G. Tadmor, and F. Thiele. A hierarchy of low-dimensional models for the transient and post-transient cylinder wake. *J. Fluid Mech.*, 497:335–363, 2003.

O. K. Rediniotis, J. Ko, and A. J. Kurdila. Reduced order nonlinear Navier-Stokes models for synthetic jets. *J. Fluids Enrng.*, 124(2):433–443, 2002.

C. Rowley, I. Mezić, S. Bagheri, P. Schlatter, and D. S. Henningson. Reduced-order models for flow control: balanced models and Koopman modes. Seventh IUTAM Symposium on Laminar-Turbulent Transition, 23-26 June 2009, Stockholm, Sweden, 2009.

P. Schmid and J. Sesterhenn. Dynamic mode decomposition of numerical and experimental data. In *61st Annual Meeting of the Division of Fluid Dynamics of the American Physical Society*, 2008.

M. Schumm. *Experimentelle Untersuchungen zum Problem der absoluten und konvektiven Instabilität in Nachlauf zweidimensionaler stumpfer Körper*. PhD thesis, HFI, TU-Berlin, 1991.

S. Siegel, K. Cohen, J. Seigel, and T. McLaughlin. Proper orthogonal decomposition snapshot selection for state estimation of feedback controlled flows. In *AIAA Aerospace Sciences Meeting and Exhibit*, January 9–12, 2006, Reno/NV, 2006. Paper 2006-1400.

L. Sirovich. Turbulence and the dynamics of coherent structures, Part I: Coherent structures. *Quart. Appl. Math.*, XLV:561–571, 1987.

P. J. Strykowski and K. R. Sreenivasan. On the formation and suppression of vortex 'shedding' at low Reynolds numbers. *J. Fluid Mech.*, 218:71–107, 1990.

G. Tadmor, O. Lehmann, B. R. Noack, and M. Morzyński. Mean field representation of the natural and actuated cylinder wake flow. *Phys. Fluids* 22 (3), 034102-1...22, 2010.

V. Theofilis. Advances in global linear instability analysis of nonparallel and three-dimensional flows. *Progress in Aerospace Sciences*, 39(4):249–315, 2003.

M. F. Unal and D. Rockwell. On the vortex formation from a cylinder; Part2. control by a splitter-plate interference. *J. Fluid Mech.*, 190:513–529, 1987.

D. Wolter, M. Morzyński, H. Schütz, and F. Thiele. Numerische Untersuchungen zur Stabilität der Kreiszylinderumströmung. *Z. Angew. Math. Mech.*, 69:T601–T604, 1989.

A. Zebib. Stability of viscous flow past a circular cylinder. *J. Engr. Math.*, 21:155–165, 1987.